

Article

Atmospheric Pressure Plasma Polymerization of Carvone: A Promising Approach for Antimicrobial Coatings

Asad Masood¹, Naeem Ahmed¹ , Fatima Shahid² , M. F. Mohd Razip Wee¹ , Anuttam Patra³
and Kim S. Siow^{1,*} 

¹ Institute of Microengineering and Nanoelectronics, Universiti Kebangsaan Malaysia, Bangi 43600, Malaysia

² Department of Applied Physics, Faculty of Science and Technology, Universiti Kebangsaan Malaysia, Bangi 43600, Malaysia

³ Chemistry of Interfaces Group, Luleå University of Technology, SE-97187 Luleå, Sweden

* Correspondence: kimsiow@ukm.edu.my

Abstract: Medical devices are often vulnerable to colonization by nosocomial pathogens (bacteria), leading to infections. Traditional sterilization methods may not always be effective, and as a result, alternative options are being explored to prevent microbial contamination. Recently, scientists are emphasizing using plant-derived essential oils that possess inherent antibacterial properties to produce antimicrobial coatings using plasma polymerization technology carried out at atmospheric pressure (AP). This approach shows promise compared to other coating strategies that need several processing steps, including a high-vacuum system, and are laborious, such as the immobilization of antimicrobial materials on precoated layers in the low-pressure plasma polymerization approach. The present study demonstrates the potential of AP plasma polymerization for producing thin films with excellent antibacterial properties and surface characteristics. The resulting coatings are stable, smooth, and have high wettability, making them ideal for repelling bacteria. The calculated zeta potential and deposition rate for the films are also favorable. These AP plasma-polymerized thin films created from carvone show a reduction rate of more than 90% for *Escherichia coli* and *Staphylococcus aureus* bacteria. Our computational docking studies also reveal strong binding interactions between the original carvone monomer and both bacteria. The study suggests that these AP plasma-produced coatings have great potential as antibacterial coatings for biomedical devices.

Keywords: atmospheric pressure plasma polymerization; antibacterial coating; carvone; ASTM E2149-20; *E. coli*; *S. aureus*



Citation: Masood, A.; Ahmed, N.; Shahid, F.; Mohd Razip Wee, M.F.; Patra, A.; Siow, K.S. Atmospheric Pressure Plasma Polymerization of Carvone: A Promising Approach for Antimicrobial Coatings. *Coatings* **2023**, *13*, 1112. <https://doi.org/10.3390/coatings13061112>

Academic Editor: Domenico Pangallo

Received: 31 March 2023

Revised: 25 May 2023

Accepted: 8 June 2023

Published: 16 June 2023



Copyright: © 2023 by the authors. Licensee MDPI, Basel, Switzerland. This article is an open access article distributed under the terms and conditions of the Creative Commons Attribution (CC BY) license (<https://creativecommons.org/licenses/by/4.0/>).

1. Introduction

Biomedical devices, such as dental implants, bronchoscopes, endoscopes, catheters, heart valves, and orthopedic scaffolds, which are used to treat various health conditions, can be colonized by nosocomial pathogens, especially the ESKAPE group of bacteria [1,2]. These devices are prone to pathogenic outbreaks caused by the adherence of bacterial proteins, polysaccharides, and biofilms. In fact, biofilm formation on medical devices is responsible for about 80% of pathogenic outbreaks [3], and these biofilms can make bacteria 100 to 1000 times more resistant to antibiotic treatment [4]. Unfortunately, the inadequate sterilization of biomedical devices using conventional regimes is very common, with reported cases as high as 56%, contributing to the spread of infections. This has led to the rapid spread of infectious diseases and is the main cause of mortality globally, in part due to both the overuse and misuse of antimicrobial agents, causing nationwide economic losses accounting for 0.4%–1.6% value of the GDP in several regions [5]. Amidst these mounting concerns regarding pathogen-triggered outbreaks, scientists are tirelessly exploring innovative therapeutic alternatives to tackle these menacing situations [6]. Using antimicrobial coatings on medical devices has shown promise as a potential solution to

combat drug-resistant pathogens and reduce the risk of secondary transmissions [7]. This approach is effective and easy to implement, which has led to a growing interest in developing antimicrobial substances that can provide patients with pathogen-free equipment while also avoiding drug resistance.

Recently, a shift toward using environmentally friendly polymers as an alternative coating material for biomedical devices has been observed. These polymers can destroy bacteria by targeting their cell membranes and can effectively assist in minimizing the negative impact of drug resistance [8]. In order to impart antibacterial characteristics to medical devices, researchers have explored the use of natural antimicrobial agents, such as essential oils and their derivatives. These agents, including terpineol, lavender oil, and linalyl acetate, have been incorporated into solid polymer coatings on surfaces [9].

In order to bind these antibacterial precursor materials, several coating strategies have been investigated for this purpose, such as atom transfer radical polymerization (ATRP) [10], self-assembled monolayers (SAMs) [11], and layer-by-layer deposition [12], as well as plasma polymerization or plasma treatment [13,14]. Particularly, plasma treatment and plasma polymerization are emerging techniques that can be distinguished from each other based on the utilization of an organic precursor in the latter process, which deposits a film of polymeric coating onto the substrate. On the other hand, plasma treatment involves the insertion of chemical moieties onto the substrate using gaseous precursors (e.g., N_2 and O_2). Both plasma-based processes offer the benefits of modifying the surface chemistry of the material without impacting its bulk characteristics and can be scaled up for reproducible quality during manufacturing. The antibacterial properties of the plasma-polymerized natural compounds are thought to result from their ability to disrupt the bacterial membranes through positive charge or their interference with quorum sensing during biofilm formation [15]. However, adequate optimization is required to achieve the necessary efficacy using such immobilization schemes, and the choice of the right precursor is vital in this regard.

Interestingly, one essential oil, R-(−)carvone, extracted from spearmint plants, tends to confer antimicrobial properties [16] to the deposited substrates. The antibacterial activity of R-(−)carvone is attributed to its monoterpene group. Hitherto, although carvone possesses a simple chemical structure to be deposited, no practical experiments have been conducted to produce their thin films via atmospheric pressure plasma polymerization (AP-PP) for antimicrobial purposes. In such an atmospheric-pressure plasma jet (APPJ) process, one electrode was grounded while the other was energized to create an electric field between them, and a gas flow between the electrodes was ionized to form a stable plasma. The carvone monomer was vaporized to this gas flow before plasma ignition to serve as the precursor for the deposited polymer coating. The resulting products, including reactive species and nonreactive ones, were deposited onto the chosen substrate, where adsorption and surface reactions occurred at the same time. Several published studies have investigated the antibacterial properties of various non-carvone coatings produced by this APPJ process [13,17].

In this study, we present this APPJ process as a fast and one-step plasma polymerization method using carvone as a precursor for producing thin films for antibacterial purposes. As far as our extensive literature survey depicts, this study presents the initial evidence of utilizing carvone's AP-PP as a potential antibacterial agent, exhibiting bactericidal effects. Unlike the previous research by Chan et al., which employed the low-pressure plasma polymerization technique requiring vacuum conditions, our approach offers a distinct methodological advantage [14]. To demonstrate the viability of the process, this study explores how altering the position of the plasma-polymerizing device affects the physicochemical properties of the resulting thin films. To address economic and environmental concerns, it is desirable to develop a straightforward and ecofriendly approach to creating antibacterial coatings. As a preliminary demonstration, our coatings created an efficient antibacterial coating against *E. coli* and *S. aureus*. The effectiveness of this AP plasma-polymerized carvone (AP-PP-Car) coating was evaluated using in vitro methods,

including field emission scanning electron microscopy (FE-SEM), atomic force microscopy (AFM), and fluorescence microscopy, as well as *in silico* methods for the original carvone monomer, such as molecular docking analysis, to assess the efficacy of the interaction between the antimicrobial coating and pathogens. Our APPJ-deposited carvone was expected to retain the reactive region of the original carvone monomers similar to the previous low-pressure plasma-polymerized carvone [14,15], and hence, the docking analysis was carried out using the original carvone monomer.

2. Materials and Methods

2.1. Materials

Carvone ($C_{10}H_{14}O$), an essential oil with 98% purity, was procured from Sigma-Aldrich (St. Louis, MO, USA) (product No.: 124931) and used without further purification. Glass slides were picked as the model substrate owing to their well-known positive control record. Every glass substrate was subjected to ultrasonic cleaning for 30 min in isopropyl alcohol (IPA), acetone, ethanol, and deionized water (DI). In this study, plasma discharge was carried out using 99.99% pure argon gas.

2.2. Experimental Setup of the AP Plasma Polymerization System

The developed AP plasma polymerization system is depicted in Figure 1. It consisted of a plasma jet (made up of a quartz tube) responsible for generating the plasma glow. A copper rod, acting as the high-voltage electrode joined to a high-voltage supply, was positioned within the quartz tube. On the outside, an electrode, made up of copper and serving as the grounded electrode, was secured around the quartz tube. To generate the plasma discharge, a power supply with an output voltage of 3 kV was utilized. The quartz tube had inner diameter of 3.0 mm and outer diameter of 5.0 mm approximately. The gap between the nozzle and the high-voltage electrode tip was kept at 20 mm during the whole experimental process.

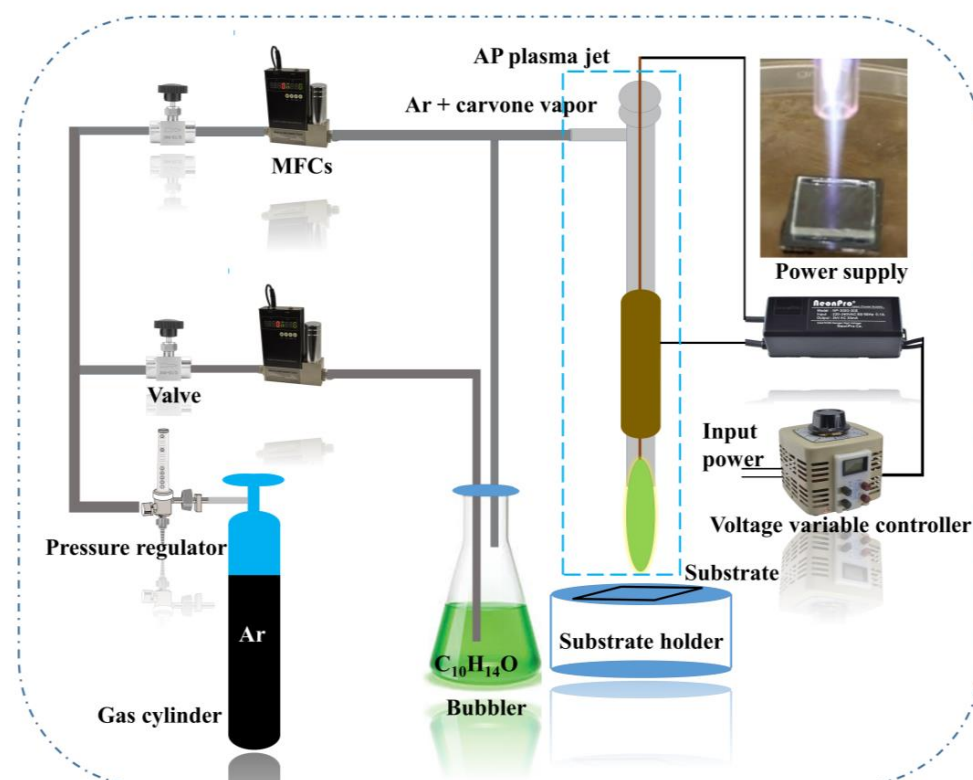


Figure 1. Schematic representation of the AP-PP-Car production setup. The inset displays the snapshot of glow discharge formed during the deposition process using the APPJ.

In the AP-PP of carvone on glass slides used as the deposition substrate, two distinct locations were used. The first location, AP1, was located 5 mm away from the nozzle and directly in the plasma glow region. The second location, AP2, was positioned 15 mm away from the nozzle and within the plasma afterglow region. The glass substrate was positioned perpendicular to the direction of gas flow. Figure 2 displays a pictorial representation of the AP-PP-Car production process, with reactive gas species passing through a neutral zone before deposition on one side and direct encounter of the reactive gas species on the other side. It is noteworthy that the optimal distance for carvone polymerization was found to be 15 mm (as shown by a dotted line) as opposed to the 5 mm distance, which could potentially etch the substrate (shown by black arrows). AP-PP-Car deposition (shown by white arrows) was carried out on 5 cm × 5 cm glass substrates, and mass flow controllers (MFCs) were employed to supply argon gas to the system. To introduce the monomer (carvone), argon gas was introduced into a bubbler containing carvone with a fixed flow rate of 130 SCCM.

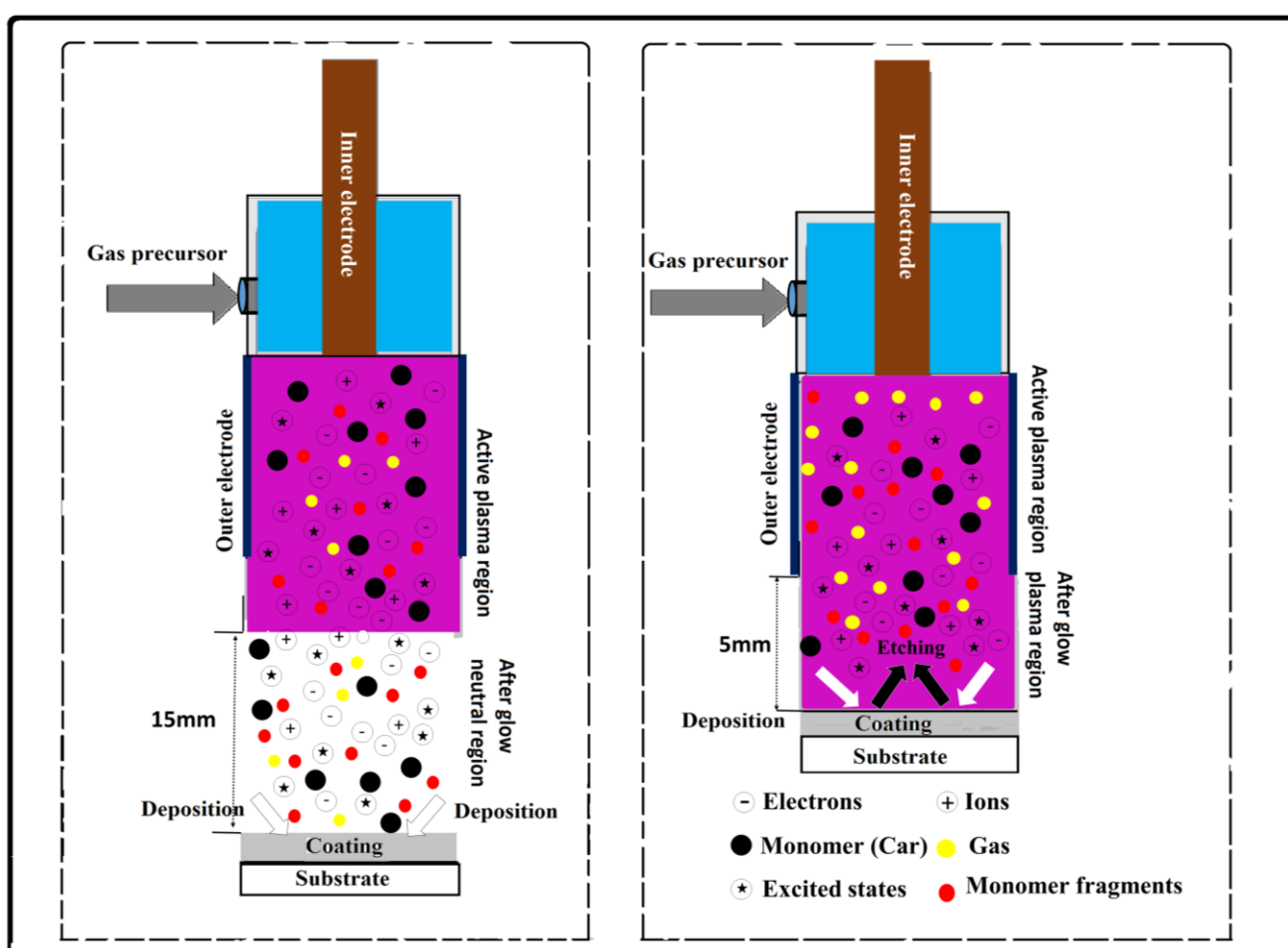


Figure 2. Pictorial representation of AP-PP-Car for two positions: AP1 glow (left) and AP2 afterglow (right).

2.3. Surface Characterization

2.3.1. Thickness and Roughness

The thickness of the AP-PP-Car was analyzed by employing a surface masking method [18]. The procedure involved dispensing 2 μ L of 10% *w/v* polystyrene in toluene onto the glass substrate, which was allowed to dry for 20 min in ambient atmospheric conditions before undergoing plasma polymerization with carvone. Subsequently, the polystyrene was removed from the surface using tweezers, and the step height was

estimated using a Bruker Dektak XT surface profiler. To ensure repeatability, the measurement process was conducted three times.

AFM was utilized for measuring the roughness of the AP-PP-Car surface and was the NEXT AFM NT-MDT model. The instrument utilized in this study operated in tapping mode, employing a silicon nitride tip, known as NSG10, with noncontact silicon gold cantilevers. The silicon nitride tip had a force constant of approximately 37 N/m and a resonant frequency of 390 kHz. To assess the average surface roughness, five different locations on each sample were scanned, covering areas of $10 \times 10 \mu\text{m}$.

2.3.2. Water Contact Angle (WCA)

The static water contact angle (WCA) of the glass substrate coated with AP-PP-Car was determined using the sessile drop method. A 2 μL droplet of milli-Q water was manually deposited on the sample, and an automated contact angle goniometer (Rame-Hart, Inc. model 100, Succasunna, NJ, USA) was used to measure the static WCA. To ensure accurate results, the measurements were conducted on three different samples prepared through separate plasma deposition cycles. Each sample was examined in three distinct regions, resulting in a total of nine measurements ($n = 9$).

2.3.3. Zeta Potential (ZP)

The electrical potential at the surface of a material when immersed in a liquid medium, known as zeta potential, can possess a significant role in estimating the biocompatibility of the material in various fields, such as biomaterials and pharmaceutical formulations.

In the present research, the ZP of the plasma-polymerized carvone was determined in DI water by utilizing 300–350 nm latex particles as tracer particles using the surface potential cell (DTS1235) and proprietary software from the Malvern Panalytical Zetasizer Nano (Malvern, UK).

2.3.4. Attenuated Total Reflectance Fourier Transform Infrared Spectroscopy (ATR-FTIR) Analysis

Chemical properties of the samples were analyzed using attenuated total reflectance Fourier transform infrared spectroscopy (ATR-FTIR). Spectra were collected in the range of 4000–600 cm^{-1} , with an average of 32 scans and a resolution of 4 cm^{-1} . A Nicolet™ iS™ 5 FTIR Spectrometer equipped with a diamond plate was utilized for the measurements. The obtained interferograms were processed using OMNIC software (version 9.8.372) to identify important peaks and correct any baseline distortions [19].

2.3.5. X-ray Photoelectron Spectroscopy (XPS)

X-ray photoelectron spectroscopy (XPS) was employed to analyze the samples using a ULVAC-PHI Quantera II instrument with an Al-K α source. The source operated at 50 W and 15 kV, with an energy of 1486 eV. Spectra were obtained at an emission angle of 45°, and each sample underwent five scan cycles. The instrument captured high-resolution spectra of C1s and N1s, achieving a resolution of 0.1 eV and a pass energy of 112 eV. Wide scan spectra were also acquired with a resolution of 1 eV and a pass energy of 280 eV.

PHI Multipak software was utilized to calculate the atomic concentration of carbon, oxygen, and nitrogen, using the survey scan spectra. For component fitting of the high-resolution spectra, CasaXPS software (version 2.3.19.1) was employed. Background subtraction of the N1s and C1s spectra was performed using the Shirley method. During component fitting, the full width at half maximum (FWHM) was constrained within the range of 1.46 eV to 1.55 eV [20,21]. The Gaussian to Lorentzian ratio was fixed at 30%. Moreover, the C1s carbon peak of the C-C and C-H bonds were calibrated at 285 eV for all C1s spectra [14].

2.3.6. Microbiological Activity

To evaluate the antibacterial performance of the AP-PP-Car thin films, the standardized test method, i.e., ASTM E2149-20, was employed. This method was used for quantifiable antimicrobial testing of non-leaching antibacterial agents [22]. Both bacteria, i.e., *E. coli* (ATTC 25927) and *S. aureus* (ATTC 25923), respectively, were selected for testing the antibacterial potential of the thin film coatings. The bacteria were grown overnight at 310 K in Luria–Bertani (LB) broth medium. An inoculum of 1×10^8 CFU/mL was prepared, and it was mixed with LB media in a ratio of 1:9 to obtain a final concentration of 1×10^7 CFU/mL. The inoculum was diluted further to 1×10^5 CFU/mL.

2.3.7. Effect on Biofilm Formation

Cultures of both bacteria (*E. coli* as well as *S. aureus*) were streaked onto nutrient agar plates and incubated overnight at 310 K. The bacterial samples were then transferred to 12-well plates and inoculated with 1×10^5 CFU/mL for 24 h to study biofilm formation. The Gram staining protocol was followed for this purpose [23]. Precisely, the samples were treated with crystal violet solution for 30 s, followed by washing with saline, and then treated with Gram iodine solution for 30 s. A decolorizer was utilized to remove weak colors, followed by a safranin stain for an additional 30 s. After staining the bacteria with safranin, any excess stain was eliminated by rinsing with a saline solution. To estimate the average surface area of the bacteria, sample images were taken at various locations using a fluorescence microscopy system (Olympus, BX53M, by Evident Corporation, Nagano, Japan) and analyzed using ImageJ[®] software (NIH and LOCI, Milwaukee, WI, USA). Each experiment was conducted three times for reliable results.

2.3.8. Field Emission Scanning Electron Microscope (FE-SEM)

The morphology of bacteria across all samples was examined using field emission scanning electron microscopy (FE-SEM) with a Zeiss Supra 55VP instrument. Sample preparation involved a process similar to biofilm formation excluding staining. After a 24 h incubation period, the samples were rinsed with a saline solution to remove any unbound biofilms. Subsequently, the samples were dried using a critical point dryer for 2 h before being imaged using FE-SEM. To mitigate surface charging, a 99.99% gold layer was applied to the samples prior to imaging.

2.3.9. Live–Dead Assay

The LIVE/DEAD[®] BacLight[™] bacterial viability kit (L7007, Invitrogen, ThermoFisher Scientific, Waltham, MA, USA) was employed to assess the viability of bacteria. To remove excess staining, the samples were immersed in 0.9% saline water prior to examination under a fluorescence microscope. Images of bacterial viability on both the AP-PP-Car and glass substrates were captured using an Olympus BX51 fluorescence microscope at a magnification of 60 \times . The red fluorescent substance, propidium iodide (PI), was detected at excitation and emission wavelengths of 490 nm and 635 nm, respectively, while the green, fluorescent substance, SYTO9, was detected at 480 nm and 500 nm. To ensure statistical validity, each sample was imaged five times as part of three replicate experiments.

2.3.10. Molecular Docking Analysis

Protein–ligand docking analysis was conducted to validate the binding affinity between bacterial proteins and selected monomer. Carvone ligand structure (ID: 7439) was extracted from the PubChem repository and converted to MOL2 format [24,25]. Due to their reported ability to participate in bacterial pathogenesis, outer membrane proteins (OMPs) were used; OMPC (PDB ID 2J1N) was selected for *E. coli*, while penicillin-binding protein 2a (PDB ID: 1VQQ) was chosen for *S. aureus* [26,27]. Protein structures were acquired from the Protein Data Bank (PDB) and cleaned for docking utilizing UCSF Chimera tool [28]. CB-dock 2 was used for ligand binding pocket detection and protein–ligand

docking [29]. Default parameters were used to dock carvone against *E. coli* and *S. aureus* proteins, respectively. Resultant scores were recorded, and complexes were visualized.

2.3.11. Statistical Analysis

The experiments were conducted in triplicates employing different samples produced with various plasma polymerization cycles. Statistical significance was assessed using ANOVA and Tukey–Kramer tests with Origin[®] Pro 8 software. A significance level of less than 0.05 was chosen to determine statistical significance.

3. Results and Discussion

3.1. Surface Studies

In the upcoming sections, the techniques used for surface analysis, namely, AFM, FE-SEM, and ZP measurements, were used to study the physical properties of these plasma-produced surfaces at the nanoscale.

3.1.1. Atomic Force Microscopy (AFM) Analysis

AFM is a powerful technique for investigating the surface topography and morphology of materials at the nanoscale. In the present study, AFM was used in the tapping mode to analyze the topography and morphology of AP-PP-Car surfaces.

The surface topographies of the AP-PP-Car thin films were analyzed using AFM measurements, providing both 2D and 3D views. Refer to Figure 3a–c for the visual representation. These findings suggest that plasma deposition morphology can significantly influence the surface roughness and thickness of the resulting AP-PP-Car films.

The AFM results depicted a complete and smooth coverage of AP-PP-Car (AP2 afterglow) on the substrate. The average roughness (Ra) as well as the root mean square roughness (Rq) values were significantly different for the AP-PP-Car surfaces prepared in AP1 (glow) and AP2 (afterglow) regions (Figure 3a,b and Table 1); higher roughness values were observed for AP1 (glow) surfaces (5.83 ± 1.41 nm and 5.02 ± 1.20 nm for Ra and Rq, respectively), and lower values were observed for AP2 (afterglow) surfaces (0.07 ± 0.01 nm and 0.08 ± 0.01 nm for Ra and Rq, respectively). In the present study, the Ra value of AP-PP-Car (AP2) was similar to that of the low-pressure-pulse plasma-polymerized carvone reported previously [15].

Table 1. Thickness, average roughness (Ra), and root mean square roughness (Rq) of AP plasma-polymerized thin film of carvone (AP-PP-Car) deposited at different positions.

Sample	Thickness (nm)	Average Roughness, Ra (nm)	Root Mean Square Roughness, Rq (nm)
AP1	41.7 ± 3.1	5.02 ± 1.20	5.83 ± 1.41
AP2	153.6 ± 1.9	0.07 ± 0.01	0.08 ± 0.01
24 h DI-water-immersed AP2	147.0 ± 2.5	0.08 ± 0.01	0.09 ± 0.02

Furthermore, based on the profilometer measurements, Figure 3d and Table 1 show that the thickness of AP-PP-Car deposited at the AP1 and AP2 positions was estimated to be about 41.7 ± 3.1 nm and 153.6 ± 1.9 nm, respectively. The thickness of the AP-PP-Car (AP2) surface was found to be approximately 3.7 times greater than that of AP-PP-Car (AP1). The deposition rate of AP2 was also much higher (approximately four times) compared to that of AP1, which resulted in the increased thickness of the resulting film.

The observed differences in the roughness and thickness values between AP1 and AP2 regions could be attributed to several factors. Firstly, the longer exposure time to the plasma jet in the afterglow region (AP2) is likely to be responsible for the smoother and more homogeneous coating, as it provided more time for the monomers to polymerize and create a uniform film. Additionally, the higher deposition rate observed in the AP2 region also contributed to the increased thickness of the resulting film. The higher roughness

values observed for AP1 surfaces might be due to the roughening influence of the plasma jet in the glow region, which caused more irregularities in the resulting film. Another possible explanation for the rougher AP1 surfaces is attributed to the direct glow ion etching, which results in less polymerization and less uniform coating compared to the afterglow regions [30]. The stability of the AP-PP-Car (AP2) surface in aqueous environments was also investigated using AFM analysis. The immersed surface depicted a small increase in roughness values and a decrease in thickness, suggesting that the surface had undergone minor degradation or leaching of incomplete oligomers. However, the small changes observed in the roughness and thickness values indicated that the AP-PP-Car (AP2) surface is still stable in aqueous environments.

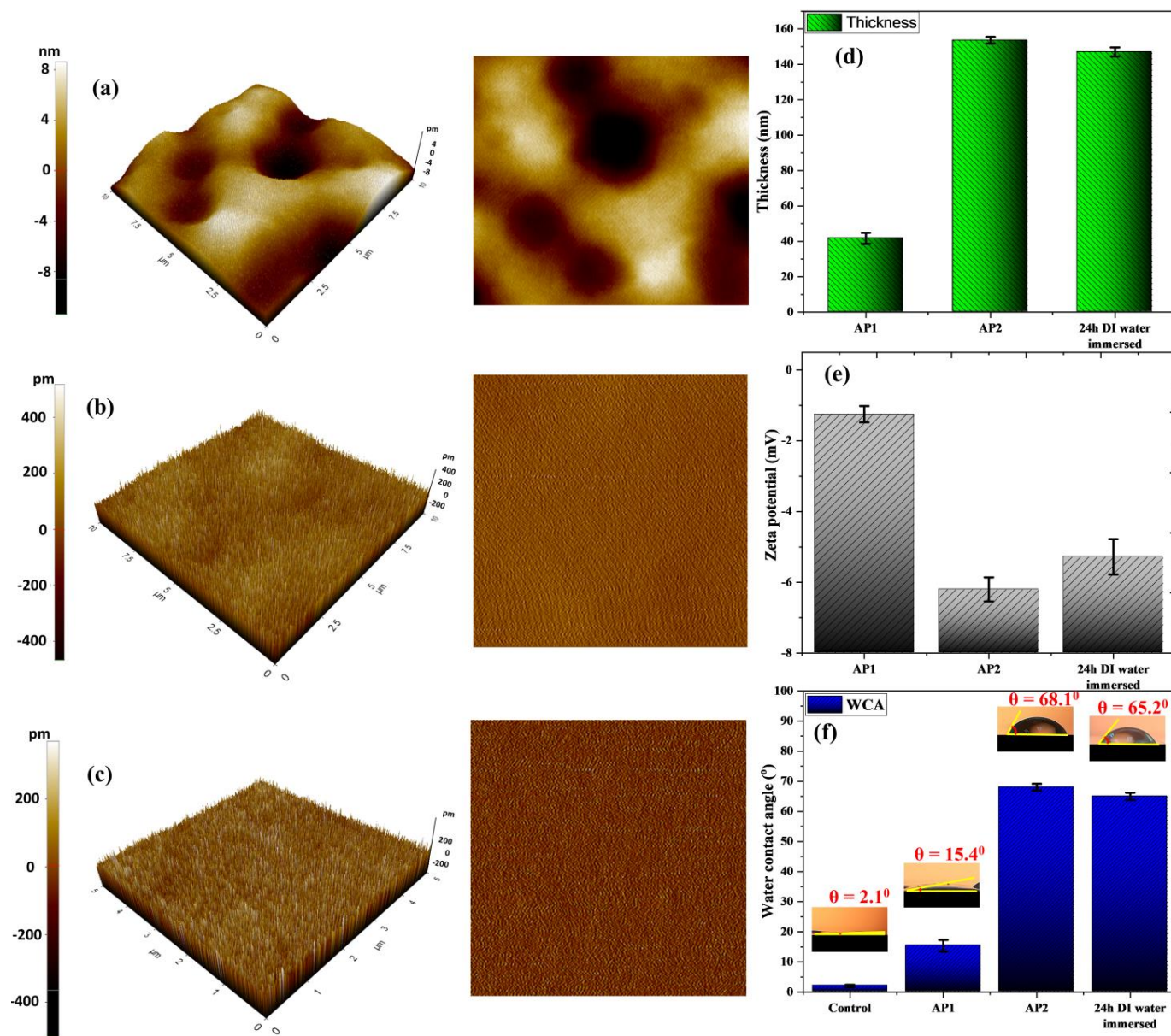


Figure 3. Two-dimensional and three-dimensional AFM images of the AP-PP-Car thin films deposited at (a) AP1, (b) AP2, and (c) 24 h DI–water–immersed AP2. (d,e) Thin film thickness (nm) and zeta potential (mV) of AP-PP-Car deposited at different positions. (f) Graph and photographs of WCA of control and AP-PP-Car with positions (AP1, AP2, and 24 h DI–water–immersed AP2) deposited on the glass substrate.

3.1.2. Zeta Potential Measurements

ZP is an important physical property that describes the surface charge of a material affecting its interactions with other materials in solution [31]. In the current research, we estimated the ZP values in the AP1 and AP2 regions, as well as after immersion in DI water for 24 h (Figure 3e).

The ZP values of AP-PP-Car in the AP1 and AP2 regions were found to be -1.25 mV and -6.20 mV, respectively. These negative zeta potential values indicated that the AP-PP-Car surfaces are negatively charged, which could be attributed to the occurrence of carboxyl groups on the surface. The higher negative ZP value in the AP2 region suggested that the more uniform coating observed in the AFM images led to the high density of carboxyl groups on the surface being successfully measured in this work.

The analysis of the AP-PP-Car (AP2) surface after immersion in DI water for 24 h showed a decrease in the zeta potential value to -5.28 mV. This decrease in the zeta potential value suggested that the surface of AP-PP-Car (AP2) was stable in aqueous environments and that the surface charge was maintained. The stability of the surface charge is an important property for applications that require long-term stability in aqueous environments.

The negative zeta potential values of AP-PP-Car (AP2) suggested that the surface may be suitable for repelling bacterial adhesion and biofilm formation [32,33]. Bacterial adhesion is often facilitated by positively charged surfaces, and the negative surface charge of AP-PP-Car (AP2) could potentially reduce bacterial adhesion and biofilm formation. This property could be beneficial in the field of biomedicine, such as for implantable medical devices, where preventing bacterial colonization and infection is critical.

3.1.3. Water Contact Angle (WCA)

The wettability of plasma-polymerized thin films was estimated employing the sessile drop technique, where the angle was measured at the triple-phase contact line between air, the water droplet, and the thin film. The adhesive forces between the liquid drop and the substrate were expected to be independent of the drop volume (provided the drop is small) [34], but the surface roughness and chemical composition could affect the droplet symmetry and contact angles [35]. Surface topography has an important part in determining the wettability of a substrate, as roughness can sometimes increase the contact angles [36]. WCA measurements provide the physical–chemical information of the outermost layer of the material, typically within the range of 0.5–1.0 nm [37].

WCA measurements were employed to probe the surface characteristics of both AP1 and AP2. The control glass sample was also tested as a comparison. The measured contact angles were $\sim 0^\circ$, 15.4° , and 68.1° for the control, AP1, and AP2 samples, respectively (Figure 3f). The significantly higher contact angle of AP2 compared to the control and AP1 suggested that the plasma polymerization process produced a relatively hydrophobic AP2 surface. The smooth, homogenous, and pinhole-free surface of AP2 further supported the formation of a hydrophobic coating because a smooth surface generally favors a lower contact angle.

Alternatively, the relatively low contact angle of AP1, the presence of cracks and holes on its surface, and its heterogeneous morphology indicated a different surface composition and morphology compared to AP2. After the immersion of AP2 in DI water for 24 h, its contact angle was measured again and found to be 65.2° , indicating a hydrophobic surface. The reduction in wettability was possibly caused by degradation or leaching of the hydrophobic oligomers from the coatings. However, the WCA value of 65.2° for AP2 remained high and still indicated a hydrophobic surface, thus suggesting the stability of the AP2 coating in an aqueous environment.

3.1.4. Field Emission Scanning Electron Microscopy (FE-SEM)

FE-SEM analysis is a useful way for investigating the surface morphology and structure of materials at high magnification. In this study, we used FE-SEM to analyze the coatings obtained from AP-PP-Car at two different positions, AP1 and AP2 (Figure 4).

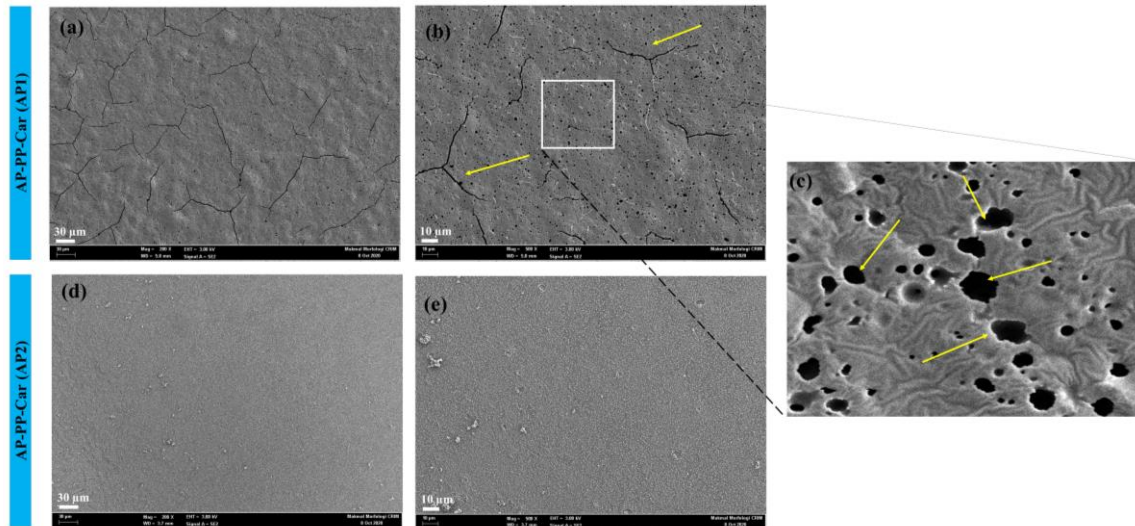


Figure 4. FE-SEM images of the AP-PP-Car thin films deposited at (a–c) AP1 and (d,e) AP2.

The coating obtained in the AP1 position (Figure 4a–c), which was in the glow region, was found to be very rough with the presence of holes and cracks (Figure 4c) [38]. Figure 4c has been generated from Figure 4b by zooming the area in white square. This roughness could be associated with the high-energy plasma present in the glow region, which can cause physical damage to the coating. The cracks and holes (indicated by yellow arrows) in the coating were likely caused by stresses during direct ion plasma deposition, which could cause the polymer chains to break or create voids in the coating.

On the other hand, the coating obtained in the AP2 position (Figure 4d,e), which was in the afterglow region, was found to be smooth and pinhole free. These smooth surfaces could be explained by the fact that the afterglow region has a lower energy plasma, which was less likely to cause physical damage to the coating [39]. Additionally, the lower energy plasma in the afterglow region might have resulted in a more uniform and dense coating, which prevented the formation of pinholes.

The FE-SEM analysis also corroborated with the AFM analysis, which showed similar results. The AFM analysis revealed that the coating obtained in the AP1 position was rougher with a higher surface roughness value, while the coating obtained in the AP2 position was smoother with a lower surface roughness value. These results provided valuable insights into the optimization of the AP-PP process for obtaining coatings with the desired surface properties.

3.2. Chemical Analysis

Following the determination of the surface topography, morphology, deposition rate, zeta potential, and WCA of the AP-PP-Car thin films, a comprehensive chemical analysis was performed to identify the chemical composition of the film surface. Chemical surface analyses were performed using FTIR and XPS. The results obtained from these analyses provide valuable insight into the relationship between the surface topography and surface chemistry, which is crucial in different applications, such as surface modification and corrosion resistance, as well as adhesion [40].

3.2.1. FTIR Analysis

The study aimed to confirm the creation of a thin film AP-PP-Car on a glass substrate. FTIR analysis was employed to detect the chemical bonds present in these plasma coatings. The ATR-FTIR spectra of the AP-PP-Car thin films and carvone monomer were compared to observe the characteristic bands corresponding to the chemical groups present in the samples (Figure 5a,b).

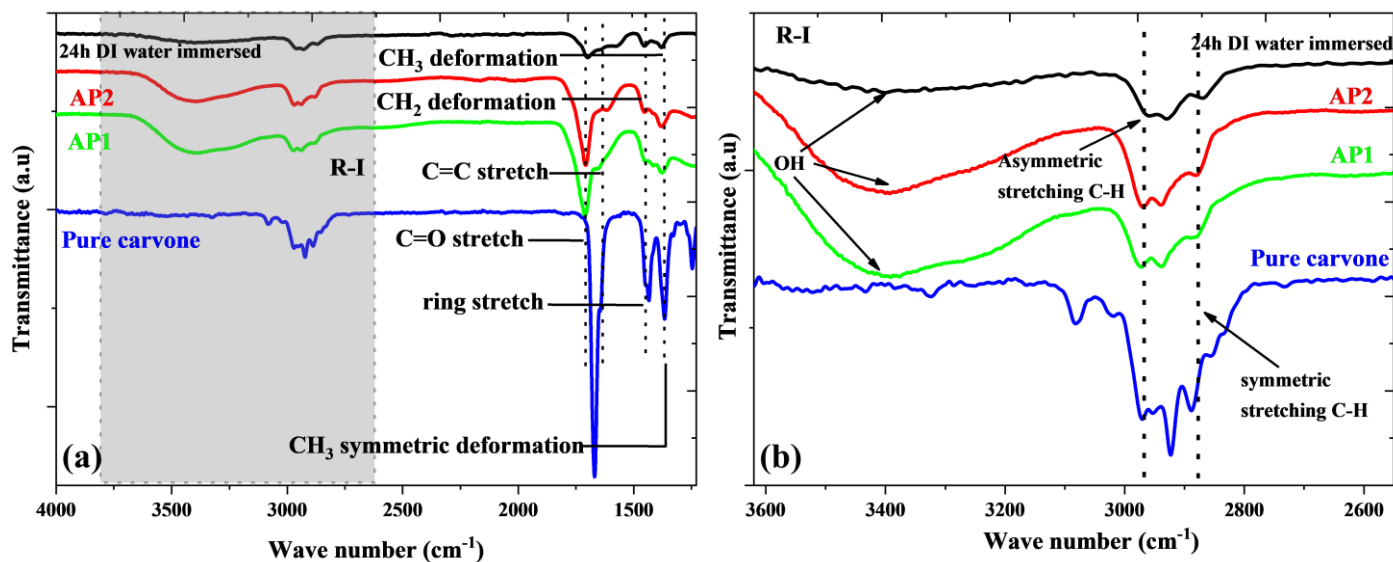


Figure 5. (a) FTIR spectra of carvone monomer and AP-PP-Car with positions (AP1, AP2, and 24 h DI–water–immersed AP2) deposited on the glass substrate and (b) a magnification of R-I regions for AP-PP-Car.

Carvone consists of various types of bonds, including C–H, C=O, C=C, and C–C bonds [41,42]. These bonds exhibit characteristic vibrational frequencies in the infrared spectrum. The symmetric stretching of C–H bonds occurs at 2834 and 2856 cm^{-1} , while the asymmetric stretching of C–H bonds was observed at 2920 and 2964 cm^{-1} . Vibrations related to unsaturated C–H bonds were found at 3010, 3046, 3072, and 3083 cm^{-1} . The asymmetric bending of C–H bonds occurred at 1436 cm^{-1} , and symmetric bending was detected at 1375 cm^{-1} . Additionally, the out-of-plane bending of C–H bonds was observed at 1310 cm^{-1} , although with low intensities. The corresponding peaks for the pure carvone monomer were observed at 1670 cm^{-1} and 1645 cm^{-1} , assigned to the conjugated -C=C-C=O (blue-colored in Figure 6a) and isolated C=C (violet-colored in Figure 6a), respectively [43]. The study suggested that plasma polymerization occurs via the -C=C- of the conjugated -C=C-C=O and not by the isolated C=C. No shift of the peak position of the later bond was observed between the pure monomer and plasma polymer. For the former, after polymerization, an increase in the bond order of the -C=O bond was observed due to the breakdown of the conjugation in the plasma polymer. In addition, during plasma treatment, a fraction of the C=O group might have been oxidized to the O–C=O group, causing the peak to shift at a higher wavenumber.

FTIR spectra analysis of AP-PP-Car, including both the AP1 and AP2 regions, revealed the presence of CH₃ and CH₂ deformation bonds at 1310 cm^{-1} and 1436 cm^{-1} , respectively, which are inherent properties of organic compounds. A weak broadband around 3340 cm^{-1} corresponding to O–H stretching was also observed (Figure 5b), resembling the chemical fingerprints of plasma-polymerized materials resulting from essential oils and their constituents [9,15]. These results validate the successful deposition of the AP-PP-Car thin film layer onto the glass substrate. The AP2 region exhibited a significantly stronger C=O bond compared to the AP1 region, indicating a higher density of carboxyl groups present on the surface, which could be attributed to the more uniform coating observed in the AFM images. During the plasma polymerization process, the free radicals present in

the plasma-polymerized films are formed either through plasma active species ablation or imperfect fragment bonding [44]. These free radicals interact with oxygen in the atmosphere, resulting in the generation of oxygenated species, particularly carboxyl groups, on the film surface [45]. The presence of carboxyl groups offers opportunities for chemical functionalization, making them potentially beneficial for applications such as drug delivery and biosensing.

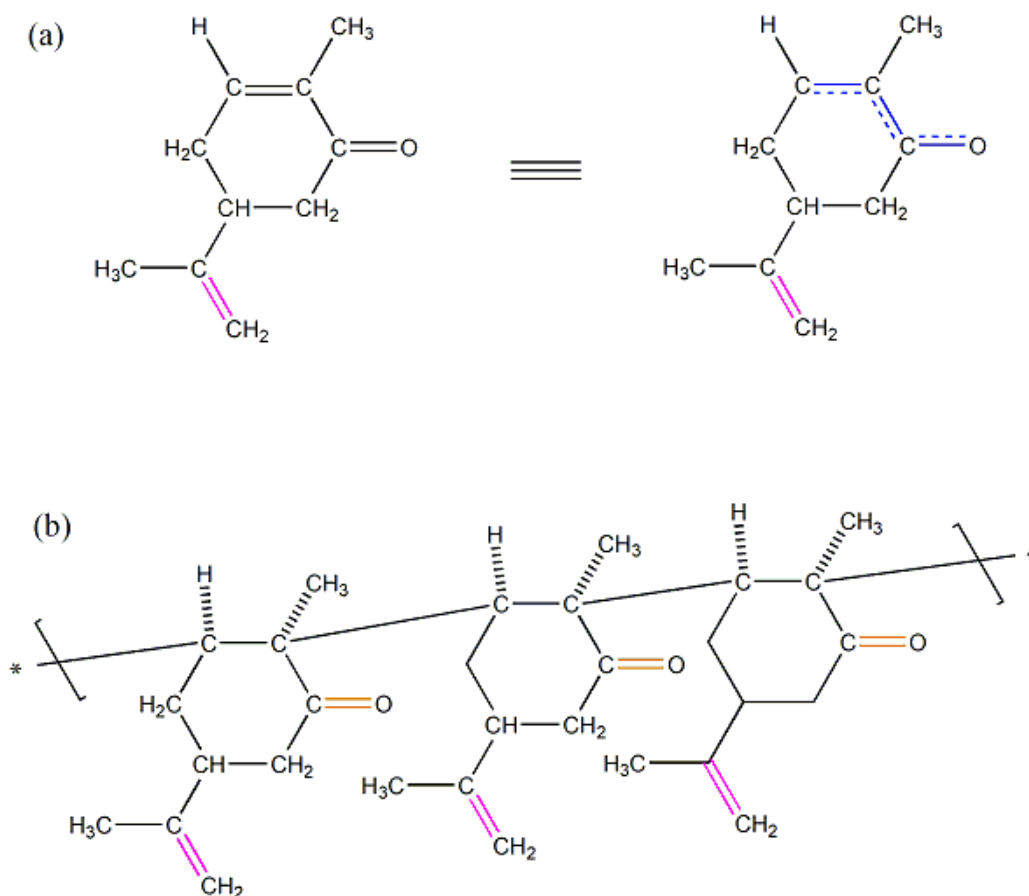


Figure 6. (a) Structure of the pure carvone monomer and (b) plausible structure of the AP-PP-Car.

FTIR analysis of the water-immersed AP2 region revealed the stability of the carvone thin film layer on the glass substrate, as all the chemical bonds detected in the AP2 region were also present in the water-immersed sample. This retention indicated that the thin film layer is resistant to degradation and can maintain its properties even after exposure to aqueous environments. The presence of C=C bonds in all three spectra (AP1, AP2, and the water-immersed AP2) suggested the presence of carvone on the thin film layer, as this C=C was a characteristic peak of carvone. The AP-PP-Car thin films in the surface phase exhibit broader and fewer noticeable bands compared to the monomer carvone due to the cross-linking ability of plasma polymers [46].

3.2.2. XPS Analysis

XPS analysis was performed to evaluate the surface chemical composition of AP-PP-Car films and to confirm the possible chemical bonding on the surfaces (Figure 7). The C1s peak was deconvoluted into four components (Figure 7a–c). The hydrocarbon bonds (C–C/C–H/C=C) with a binding energy of 285 eV formed the polymer backbone. Chemical groups, such as hydroxyl (C–O–H)/ether (C–O–C), carbonyl (C=O), and carboxyl (O–C=O) with binding energies of 286.4 eV, 287.7 eV, and 289.0 eV, respectively, were incorporated into the polymer matrix. The presence of C–O, C=O, C=C, and O–C=O

bonds indicated that AP-PP-Car had undergone partial oxidation, and the results were consistent with the earlier reported Fourier transform infrared (FTIR) spectra.

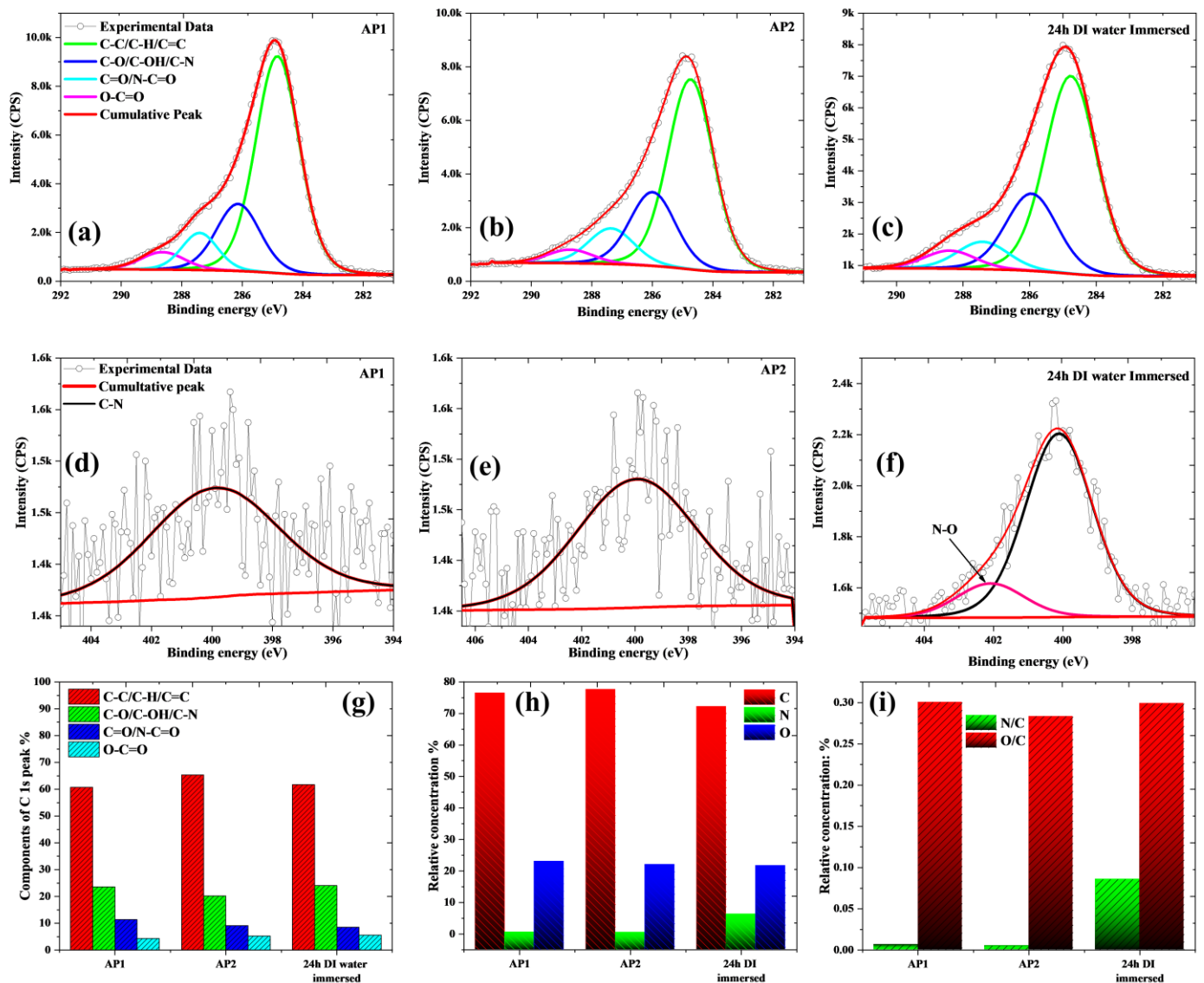


Figure 7. (a–f) Component-fitted C1s spectra and N1s spectra for AP-PP-Car at various positions (AP1, AP2, and water-immersed AP2). (g) The relative concentration of components (AP-PP-Car) in curve-fitted C1s, (h) relative atomic concentration of C, O, and N, and (i) ratio of oxygen to carbon (O/C) and nitrogen to carbon (N/C).

Surface chemical composition analysis of the AP-PP-Car films was conducted using XPS to investigate potential chemical bonding on the surfaces (refer to Figure 7). The C1s peak was deconvoluted into four components (Figure 7a–c). The polymer backbone consisted of hydrocarbon bonds (C–C/C–H/C=C) with a binding energy of 285 eV. Within the polymer matrix, chemical groups such as hydroxyl (C–O–H)/ether (C–O–C), carbonyl (C=O), and carboxyl (O–C=O) were incorporated, exhibiting binding energies of 286.4 eV, 287.7 eV, and 289.0 eV, respectively [47]. These findings indicated that partial oxidation had occurred in the AP-PP-Car film, which aligned with the earlier reported Fourier transform infrared (FTIR) spectra and confirmed the presence of C–O, C=O, C=C, and O–C=O bonds.

Figure 7d–f also show the minute presence of nitrogen moieties in the AP-PP-Car thin film. This could be attributed to the presence of nitrogen in the air being ionized together during plasma deposition. The XPS analysis of AP2 immersed in water showed the presence of various N bonds, indicating the stability of these thin films. After aqueous immersion, the nitrogen percentage, as well as the nitrogen-to-carbon ratio, increased (Figure 7f,h,i). The presence of amide bonds in the immersed carvone thin film was likely to be caused by the oxidation of the amine groups, but the overall increase in nitrogen moieties was somewhat puzzling and will be investigated further.

These results are in line with previous research conducted on plasma-polymerized natural oils [47,48]. To determine the relative concentrations of different carbon bonding states in relation to the overall carbon concentration in the sample, Gaussian curve fitting was employed. The distribution of different groups within the C1s peak is illustrated in Figure 7g. The analysis of AP2 revealed the following values: hydrocarbon species accounted for 65.37% of the total carbon and represented the backbone of the coatings, reflecting the chemical bonds present in carvone. In comparison to previous studies utilizing AP plasma [49], hydrocarbons (C–C/C–H) were the dominant component in this coating composition. The second-largest contribution came from C–O groups, comprising 20.21% of the total, while C=O and O–C=O groups contributed 9.15% and 5.27%, respectively, to the overall composition. The percentage of the hydrocarbon species of AP1 (60.72%) was relatively low compared to AP2. Overall, the carbon percentage was also high in AP2 (Figure 7h).

The percentage of C–C and O–C=O bonds was higher in the afterglow region (AP2) compared to the glow region (AP1) (Figure 7g), indicating that the plasma process continued to modify the chemical structure of the coating in AP2, possibly leading to an increase in cross-linking and branching in the polymerized structure. The carbon concentration was also greater in AP2 compared to AP1, suggesting a highly dense structure in the afterglow region, which could improve the mechanical and barrier properties of the thin film. The FTIR analysis and AFM images correlated with the XPS results, showing higher cross-linking density and smoother surface morphology in AP2 compared to AP1. These findings were consistent with earlier tests in this study that afterglow regions produce stronger chemical bonds in the plasma-polymerized coatings.

3.3. Antibacterial Evaluation of AP-PP-Car

The AP-PP-Car thin film was explored for its antimicrobial properties, and previous research has demonstrated that the antimicrobial activity of carvone may be attributed to its ability to disrupt bacterial outer membranes and inhibit the synthesis of bacterial cell walls. Furthermore, the thin films have excellent mechanical strength and stability, rendering them appropriate for use in biomedical applications [14]. This study aimed to evaluate the antibacterial efficacy of the AP-PP-Car thin film against both Gram-negative (*E. coli*) and Gram-positive (*S. aureus*) bacteria, which are known to cause biofouling.

3.3.1. Antibacterial Activity Using FE-SEM

Contact-active antibacterial coatings consist of active agents, such as organic compounds or metals, that interact with bacterial cell surfaces. These agents can disrupt the bacterial cell membrane either by directly destroying it or interfering with the membrane proteins' normal functions [50–52]. This hypothesis was tested in this study by comparing the growth of *E. coli* and *S. aureus* on control substrates versus AP-PP-Car-coated substrates.

The antimicrobial performance of AP-PP-Car thin films in the AP2 region against *E. coli* and *S. aureus* bacteria is shown in Figure 8. It demonstrates differences in the cell morphology of *E. coli* and *S. aureus* when incubated on the control and AP-PP-Car samples. When *E. coli* (Figure 8a,b) and *S. aureus* (Figure 8e,f) were incubated on the control substrate, intact cells and biofilms were observed. However, treatment with the antibacterial coating resulted in elongated and distorted *E. coli* cells, as shown in Figure 8c,d. The images also highlight ruptured *E. coli* cell envelopes, impaired cell envelopes, and cytoplasmic

membranes (Figure 8d), possibly due to carvone interfering with the bacterial lipid bilayers and proteins. *S. aureus* also experienced cell damage upon interaction with AP-PP-Car, resulting in cell death and the disruption of cell signaling pathways, as shown in Figure 8g,h. Figure 8h depicts ruptured bacterial cell walls, indicated by yellow arrows. The untreated sample showed clusters of *S. aureus* cells aggregated together (Figure 8e,f), while isolated bacterial cells were observed in the treated sample (Figure 8g).

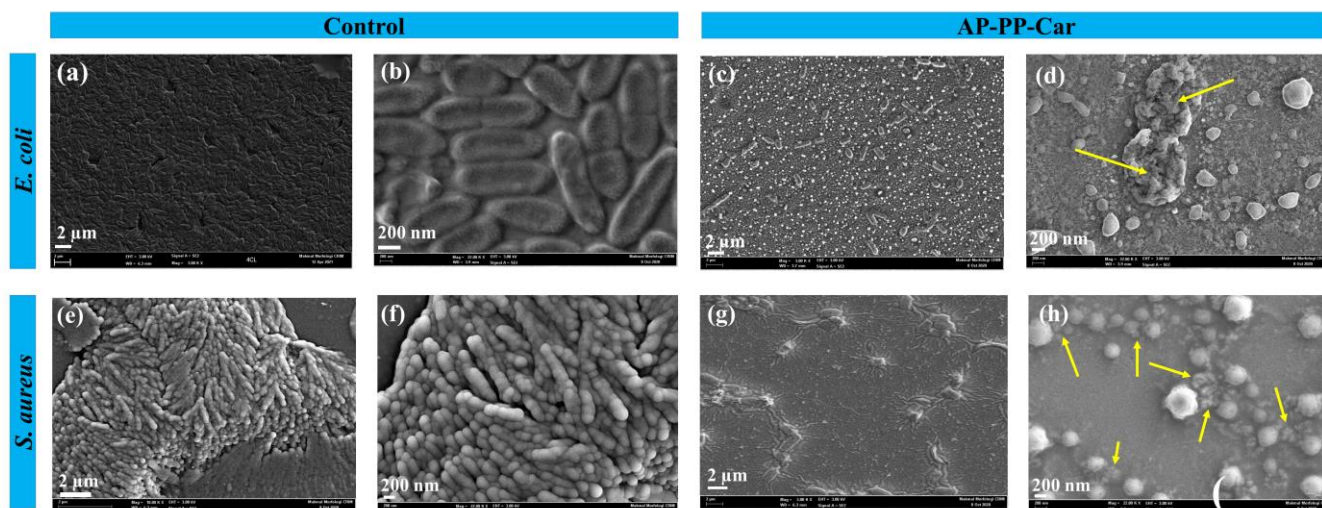


Figure 8. FE-SEM images of treated *E. coli* (a,b) and *S. aureus* (e,f) on the control and (c,d,g,h) on the AP-PP-Car thin film.

Possibly, carvone interfered with the proteins and nucleic acids needed for bacterial growth and survival, leading to its bactericidal activity. The chemical bonds (C=O, C-C, C-H, and C=C) present in the AP-PP-Car thin film may be responsible for this activity, as indicated by the XPS and FTIR results. The presence of these bonds may, therefore, be linked to the antibacterial properties of the coating.

3.3.2. Bacterial Enumeration Using Gram Staining

Bacterial staining is a valuable technique for obtaining images of cell morphology and composition, which can be further analyzed. Our FE-SEM results showed the effect of AP-PP-Car thin films on bacterial morphology and composition. To determine the number of bacterial cells retained after treatment, we performed Gram staining. We also conducted bacterial count and biofilm assays to assess the adherence of *E. coli* and *S. aureus* to both the control and AP-PP-Car-treated surfaces.

The images acquired using Gram staining (Figure 9a–d) for *E. coli* (Figure 9a,c) and *S. aureus* (Figure 9b,d) were used to conduct further calculations for enumeration. The results showed that the AP-PP-Car treatment significantly affected the bacterial count. For *E. coli*, the number of colonies was reduced from $8.15 \times 10^5 \pm 2.6 \times 10^4 \text{ cm}^{-2}$ in the control sample to $4.65 \times 10^4 \pm 1.3 \times 10^3 \text{ cm}^{-2}$ for the AP-PP-Car coatings after a 24 h incubation. Similarly, for *S. aureus*, the number of colonies was reduced from $7.63 \times 10^5 \pm 1.5 \times 10^4 \text{ cm}^{-2}$ in the control samples to $6.25 \times 10^4 \pm 3.5 \times 10^3 \text{ cm}^{-2}$ after treatment with AP-PP-Car, as shown in Figure 9i. These results clearly indicate a significant reduction in the bacterial count after interaction with the film, as seen in Figure 9j. To determine the extent of bacterial growth and attachment hindrance, we calculated the reduction percentage, which was 94.2% for *E. coli* and 91.9% for *S. aureus*. This value significantly surpasses the previously reported (low-pressure plasma-polymerized carvone) reduction efficacy of 86% and 84% [14]. The significant reduction in bacterial count achieved in this study is a new finding. This outcome suggests the formulation of a promising antibacterial regime that may have the potential for use in various biomedical applications in the future.

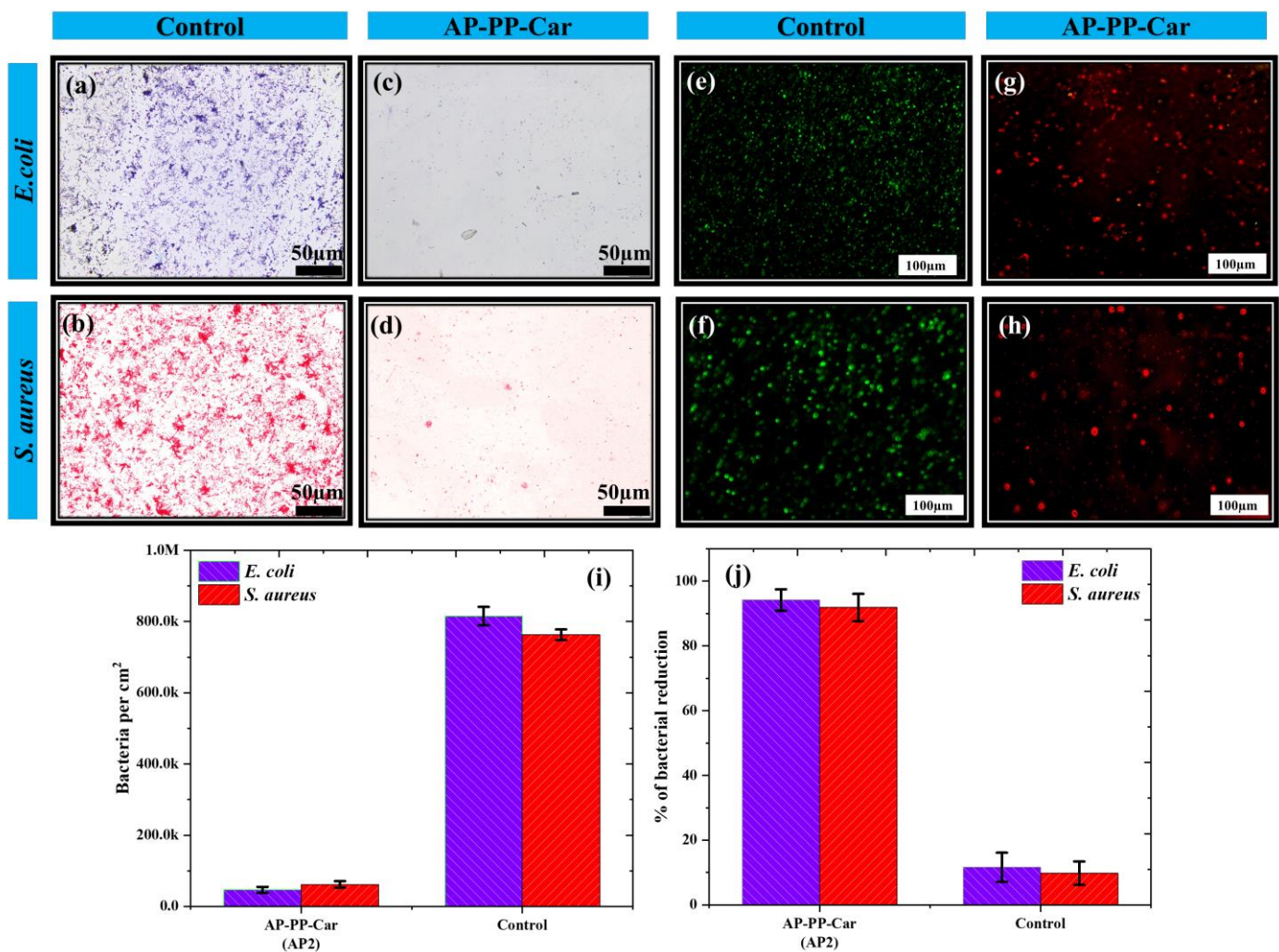


Figure 9. Fluorescent microscopic imaging of treated and stained *E. coli* and *S. aureus* on the (a,b) control and (c,d) AP-PP-Car (AP2) thin film, respectively. Live and dead bacteria are shown as green and red. *E. coli* and *S. aureus* attached on (e,f) control and (g,h) AP-PP-Car thin film, respectively. (i,j) Amount and bacterial reduction percentage of *E. coli* and *S. aureus* on control and AP-PP-Car thin film, respectively.

3.3.3. Live–Dead Assay

To evaluate bacterial adhesion and subsequent biofilm formation, fluorescence microscopy was used to observe bacterial cells incubated on the AP-PP-Car coatings. The live–dead assay was performed using PI stain to detect the dead bacterial cells. After incubation with the stain for 24 h, dead bacterial cells were observed under fluorescence as the stain binds to nucleic acids in the nucleus of compromised bacterial cells, staining them red. Live bacteria, on the other hand, were stained with SYTO9, a membrane-permeable green dye [53].

Figure 9e,f depict the pathogenic bacteria *E. coli* and *S. aureus* attached to a clean glass substrate, while the red spots in Figure 9g,h represent the dead bacteria after being treated with AP-PP-Car. This live–dead assay provided valuable information regarding the antibacterial properties of AP-PP-Car and its potential use in biomedical applications. It is imperative to acknowledge that the adhesion of biofilms may be influenced by factors beyond surface reactivity. The variability in biofilm adhesion could be attributed to the synergistic effects of various factors, such as decreased adhesion or the disruption of intercellular signaling and communication, which could impact the contact of bacteria with the surface [54].

In summary, these results demonstrated that AP-PP-Car exhibits significant antimicrobial activity against both *E. coli* and *S. aureus*. These antimicrobial properties may be attributed to the presence of bioactive compounds in carvone or the physical properties of the plasma-polymerized thin films themselves. The films altered the surface properties of the original glass substrate to reduce bacterial adhesion and growth. It is also possible that the bioactive monomers in the films leaked and interacted with the bacterial cells, leading to their demise or inhibition. These findings suggest that these films have the potential for use in biomedical applications to prevent bacterial adhesion and biofilm formation. However, further research was needed to elucidate further the mechanisms underlying the antimicrobial activity and optimize the design of the films for specific applications.

3.3.4. Computational Studies

Molecular docking studies were conducted to confirm the interactions between carvone and the bacterial proteins, with a stronger interaction indicating better bonding and the potential to initiate antibacterial pathways [55]. One PDB structure was used, that of osmoporin C (OMPC), an outer membrane protein found specifically in Gram-negative bacteria (*E. coli*) and responsible for the pathogenesis and virulence of these organisms [56]. The molecular weight of this protein structure was 117.03 kDa, with an atomic count of 8802 and a calculated residue count of 1038. The structure was obtained through X-ray diffraction at a resolution of 2 Å [57].

The chemical structures of carvone (ID: 7439) were docked to the above-mentioned protein structures, respectively [58]. Their structures are illustrated in Figure 10a. The results showing interaction affinities are shown in Table 2.

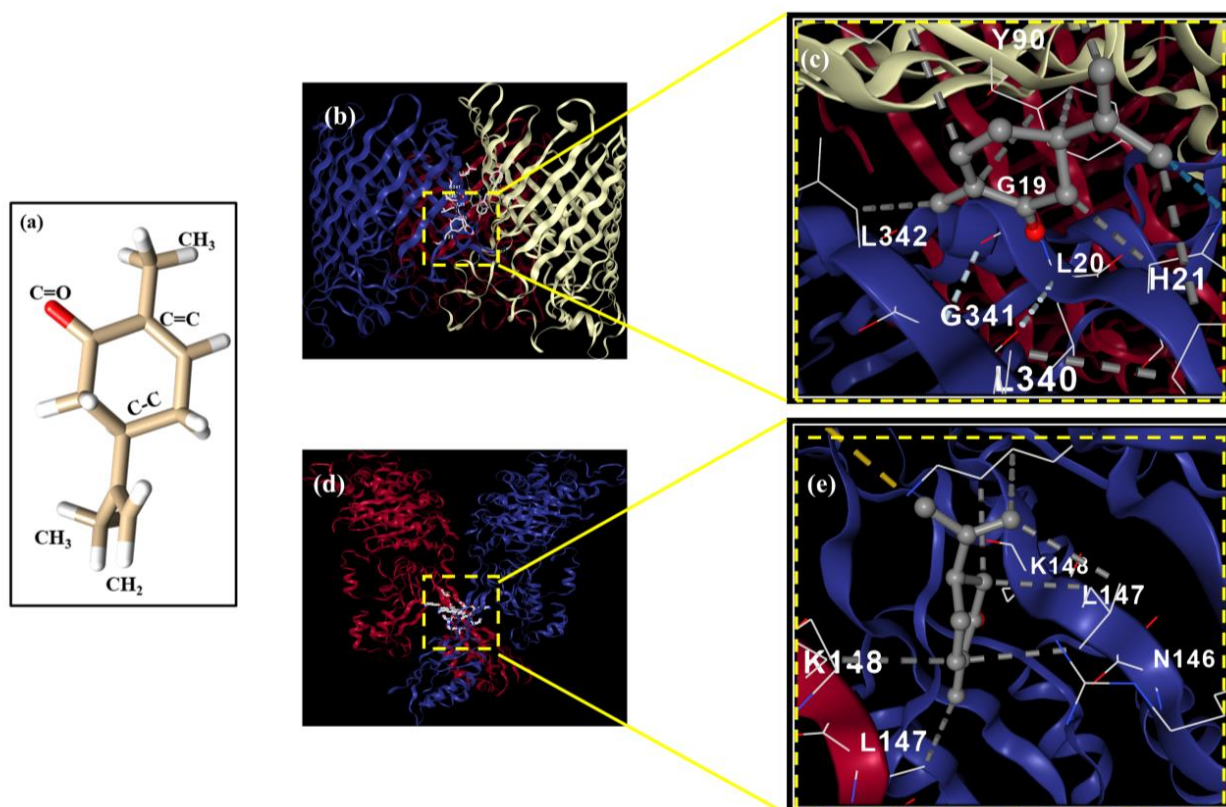


Figure 10. Three-dimensional structures of *E. coli* and *S. aureus* proteins complexed to carvone. (a) Structure of carvone. (b,d) Overall complex of *E. coli* and *S. aureus* proteins with carvone. (c,e) Magnified image of interaction pocket between *E. coli* and *S. aureus* proteins with carvone.

Table 2. Detailed summary of interactions between *E. coli* and *S. aureus* proteins with carvone monomer based on docking studies.

Monomer vs. Bacteria	Pocket ID	Vina Score	Cavity Volume (Å ³)	Center (x, y, z)	Docking Size (x, y, z)	Contact Residues
Carvone vs. <i>E. coli</i>	C1	−7.0	936	31, 8, 32	29, 17, 17	PHE88 TYR90 ALA129 GLY19 LEU20 HIS21 PHE23 LEU340 GLY341 LEU342
	C2	−5.8	821	25, 28, −6	30, 17, 17	GLY19 LEU20 HIS21 PHE23 LEU340 GLY341 LEU342 PHE88 TYR90 ALA129
	C3	−6.0	749	37, −13, −4	30, 17, 17	PHE88 TYR90 ALA129 TYR149 GLY19 LEU20 HIS21 PHE23 LEU340 GLY341 LEU342
	C4	−4.5	596	16, 27, 9	26, 17, 17	LYS16 ASP18 VAL106 LEU107 PRO108 GLN264 THR303 TYR305 SER311 TYR313 VAL343
	C5	−4.5	574	24, −5, 26	24, 17, 17	GLN266 GLY270 ARG272 TYR305 ASN307 LYS308 ASN309 GLN34
Carvone vs. <i>S. aureus</i>	C1	−6.7	6477	8, 38, 31	35, 29, 32	ASN146 LEU147 LYS148 GLU150 GLU239 ARG298 LYS317 LYS318
	C2	−4.9	3793	1, 37, 57	17, 30, 28	LEU155 ASP323 ILE324 GLN325 ASP552 LYS153 LEU155 ASN159 GLU161 ASP323
	C3	−4.9	2623	−1, 32, 8	17, 29, 17	ARG110 ASN111 HIS311 VAL174 LYS176 ASN177 ASP209 PHE211 THR234
	C4	−5.1	2139	34, 40, 18	17, 24, 17	LYS176 ASP208 ASP209 ARG110 ASN111 VAL112 GLN113 ASN115 ASP128 SER130 GLY135
	C5	−5.2	1450	28, 25, 80	17, 28, 28	TYR344 THR399 SER400 GLN521 ALA601 GLU602 LEU603 LYS604 ILE614 ASN632 LYS634

CB-Dock2 predicted five different binding pockets for each interaction, labeled C1 to C5, with varying scores. Only the highest scoring interactions were discussed to provide a better understanding of the stronger interactions [29]. The AutoDock Vina scores depend on various factors, such as the size and complexity of the ligand and receptor molecules, the binding site being considered, and the desired level of precision or accuracy. Typically, lower scores indicate a higher predicted binding affinity, meaning that there is a stronger interaction between the receptor and ligand [59].

In our analysis, the AutoDock scores indicated that for the highest-scoring interaction (C1), carvone and the *E. coli* protein had a score of −7.0, covering a binding cavity volume of 936 Å³, with docking sizes of 29, 17, and 17 for the x, y, and z coordinates, respectively. The center of the search space for these coordinates was 31, 8, and 32 Å, respectively. Ten protein residues from different portions of the protein structure were involved in binding to carvone, as shown in Figure 10b,c. Figure 10b displays the overall protein–ligand complex, while Figure 10c depicts a magnified image of the ligand binding pocket, where the yellow square highlights the interaction site. Hydrophobic bonds were observed between the ligand and protein. Carvone had the potential to bind four more cavities, with a lesser Vina score, and the overall cavity binding potential was in the following order: C1 > C3 > C2 > C4 = C5; C1 had the highest probability of carvone binding, while C4 and C5 had lower but similar probability scores, and their docking coordinates were variable.

Similarly, the interaction between the *S. aureus* protein and carvone was observed, as shown in Figure 10d,e. Figure 10d displays the overall protein–ligand complex, while Figure 10e depicts a zoomed image of the ligand binding pocket, where the yellow square highlights the interaction site. The highest interaction of the carvone monomer was again found in the C1 cavity, with a Vina score of 6.7, covering a cavity volume of 6477 Å³.

Eight protein residues from C1 were prominently bound to the carvone molecules and were predicted to form hydrophobic interactions. The docking sizes for the x, y, and z coordinates were taken as 35 Å³, 29 Å³, and 32 Å³, respectively, and the center of the search space for these coordinates was 8 Å³, 38 Å³, and 31 Å³, respectively. The overall cavity binding potential was in the following order: C1 > C5 > C4 > C2 = C3; C1 had the highest probability of carvone binding, while C2 and C3 had lower but similar probability scores, and their docking coordinates were variable. All hydrophobic interactions are illustrated by the dotted grey lines in Figure 10. The interacting residues were linked to the ligand by C-H bonds, while C=C bonds were also prominent in this interaction. It is worth noting that these C=C bonds were retained in AP-PP-Car, and C-H bonds were ubiquitous in these coatings. The FTIR, as well as XPS, results of AP-PP-Car notably depict the presence of these bonds.

4. Conclusions

In conclusion, this study showed the potential of AP-PP in producing thin films with surface properties suitable for antibacterial applications from natural products, such as carvone. A plasma jet was developed to operate at AP, and the resulting thin film exhibited excellent antibacterial properties and surface characteristics, as evidenced by the biological tests, FTIR and XPS analyses. The prepared coatings remained stable after being immersed in water for a day, and the FTIR and XPS analyses showed that the inherent bonds of the monomer were retained as well. The thin film surface was smooth and relatively hydrophobic, as determined using AFM and WCA. The measured ZP indicated a negative surface charge, which is desirable for repelling bacteria. The coating caused a reduction of more than 90% for the two pathogens *E. coli* and *S. aureus*, indicating that the plasma-polymerized thin films were effective against both Gram-positive and Gram-negative bacteria. In addition, computational docking studies between the outer membrane proteins of pathogens and the carvone monomer revealed strong binding interactions, including hydrophobic linkages. Overall, the study suggested that AP-PP-Car thin films have potential as antibacterial coatings. Future studies will involve the investigation of the binding interactions between the plasma-polymerized layer and the bacteria.

Author Contributions: Conceptualization, A.M. and K.S.S.; methodology, A.M. and K.S.S.; software, A.M. and F.S.; validation, A.M., F.S., K.S.S. and A.P.; formal analysis, A.M., A.P. and K.S.S.; investigation, A.M. and N.A.; resources, M.F.M.R.W.; data curation, A.M. and F.S.; writing—original draft preparation, A.M. and F.S.; writing—review and editing, A.P. and K.S.S.; visualization, A.M. and F.S.; supervision, K.S.S.; project administration, A.M. and K.S.S.; funding acquisition, K.S.S. All authors have read and agreed to the published version of the manuscript.

Funding: The authors express their gratitude for the financial support provided by Universiti Kebangsaan Malaysia grant GUP-2022-071 for this study. They would also like to extend their special thanks to the research officers at the Centre for Research and Instrumentation Management (CRIM) Centralized Lab, UKM, Malaysia, for their valuable technical assistance. Additionally, AP acknowledges the financial support from PRECISE LTU.

Institutional Review Board Statement: Not applicable.

Informed Consent Statement: Not applicable.

Data Availability Statement: The data used to support the findings of this study are available from the corresponding authors upon reasonable request.

Acknowledgments: The authors would like to acknowledge the financial support provided by the grant GUP-2022-071 from Universiti Kebangsaan Malaysia for this research. They extend their special appreciation to the research officers at the Centre for Research and Instrumentation Management (CRIM) Centralized Lab, UKM, Malaysia, for their valuable technical assistance. Furthermore, AP expresses gratitude for the financial support received from PRECISE LTU.

Conflicts of Interest: The authors declare no conflict of interest.

References

1. Francolini, I.; Donelli, G.; Crisante, F.; Taresco, V.; Piozzi, A. Antimicrobial Polymers for Anti-biofilm Medical Devices: State-of-Art and Perspectives. In *Biofilm-Based Healthcare-Associated Infections: Volume II*; Donelli, G., Ed.; Springer International Publishing: Cham, Switzerland, 2015; pp. 93–117.
2. Kamaruzzaman, N.F.; Tan, L.P.; Hamdan, R.H.; Choong, S.S.; Wong, W.K.; Gibson, A.J.; Chivu, A.; Pina, M.d.F. Antimicrobial polymers: The potential replacement of existing antibiotics? *Int. J. Mol. Sci.* **2019**, *20*, 2747. [[CrossRef](#)]
3. Kumar, M.; Patel, A.K.; Shah, A.V.; Raval, J.; Rajpara, N.; Joshi, M.; Joshi, C.G. First proof of the capability of wastewater surveillance for COVID-19 in India through detection of genetic material of SARS-CoV-2. *Sci. Total Environ.* **2020**, *746*, 141326. [[CrossRef](#)]
4. Patel, B.; Mishra, S.; Priyadarsini, I.K.; Vavilala, S.L. Elucidating the anti-biofilm and anti-quorum sensing potential of selenocystine against respiratory tract infections causing bacteria: In Vitro and in silico studies. *Biol. Chem.* **2021**, *402*, 769–783. [[CrossRef](#)]
5. Smith, R.D.; Yago, M.; Millar, M.; Coast, J. Assessing the macroeconomic impact of a healthcare problem: The application of computable general equilibrium analysis to antimicrobial resistance. *J. Health Econ.* **2005**, *24*, 1055–1075. [[CrossRef](#)] [[PubMed](#)]
6. Naz, A.; Obaid, A.; Shahid, F.; Dar, H.A.; Naz, K.; Ullah, N.; Ali, A. Chapter 16—Reverse vaccinology and drug target identification through pan-genomics. In *Pan-Genomics: Applications, Challenges, and Future Prospects*; Barh, D., Soares, S., Tiwari, S., Azevedo, V., Eds.; Academic Press: Cambridge, MA, USA, 2020; pp. 317–333. [[CrossRef](#)]
7. Francolini, I.; Vuotto, C.; Piozzi, A.; Donelli, G. Antifouling and antimicrobial biomaterials: An overview. *APMIS* **2017**, *125*, 392–417. [[CrossRef](#)] [[PubMed](#)]
8. Riga, E.K.; Vöhringer, M.; Widayana, V.T.; Lienkamp, K. Polymer-Based Surfaces Designed to Reduce Biofilm Formation: From Antimicrobial Polymers to Strategies for Long-Term Applications. *Macromol. Rapid Commun.* **2017**, *38*, 1700216. [[CrossRef](#)]
9. Jacob, M.V.; Easton, C.D.; Anderson, L.J.; Bazaka, K. RF plasma polymerised thin films from natural resources. *Proc. Int. J. Mod. Phys. Conf. Ser.* **2014**, *32*, 1460319. [[CrossRef](#)]
10. Coessens, V.; Pintauer, T.; Matyjaszewski, K. Functional polymers by atom transfer radical polymerization. *Prog. Polym. Sci.* **2001**, *26*, 337–377. [[CrossRef](#)]
11. Ulman, A. Self-Assembled Monolayers of 4-Mercaptobiphenyls. *Acc. Chem. Res.* **2001**, *34*, 855–863. [[CrossRef](#)]
12. Oliveira, M.B.; Hatami, J.; Mano, J.F. Coating Strategies Using Layer-by-layer Deposition for Cell Encapsulation. *Chem.—Asian J.* **2016**, *11*, 1753–1764. [[CrossRef](#)]
13. Masood, A.; Ahmed, N.; Razip Wee, M.F.M.; Patra, A.; Mahmoudi, E.; Siow, K.S. Atmospheric Pressure Plasma Polymerisation of D-Limonene and Its Antimicrobial Activity. *Polymers* **2023**, *15*, 307. [[CrossRef](#)] [[PubMed](#)]
14. Chan, Y.W.; Siow, K.S.; Ng, P.Y.; Gires, U.; Majlis, B.Y. Plasma polymerized carvone as an antibacterial and biocompatible coating. *Mater. Sci. Eng. C* **2016**, *68*, 861–871. [[CrossRef](#)]
15. Masood, A.; Ahmed, N.; Mohd Razip Wee, M.F.; Haniff, M.A.S.M.; Mahmoudi, E.; Patra, A.; Siow, K.S. Pulsed plasma polymerisation of carvone: Characterisations and antibacterial properties. *Surf. Innov.* **2022**, *40*, 1–13. [[CrossRef](#)]
16. Amirrah, I.N.; Zulkiflee, I.; Mohd Razip Wee, M.F.; Masood, A.; Siow, K.S.; Motta, A.; Fauzi, M.B. Plasma-Polymerised Antibacterial Coating of Ovine Tendon Collagen Type I (OTC) Crosslinked with Genipin (GNP) and Dehydrothermal-Crosslinked (DHT) as a Cutaneous Substitute for Wound Healing. *Materials* **2023**, *16*, 2739. [[CrossRef](#)] [[PubMed](#)]
17. Ma, C.; Wang, L.; Nikiforov, A.; Onyshchenko, Y.; Cools, P.; Ostrikov, K.; De Geyter, N.; Morent, R. Atmospheric-pressure plasma assisted engineering of polymer surfaces: From high hydrophobicity to superhydrophilicity. *Appl. Surf. Sci.* **2021**, *535*, 147032. [[CrossRef](#)]
18. Hartley, P.G.; Thissen, H.; Vaithianathan, T.; Griesser, H.J. A surface masking technique for the determination of plasma polymer film thickness by AFM. *Plasmas Polym.* **2000**, *5*, 47–60. [[CrossRef](#)]
19. Ahmed, N.; Masood, A.; Siow, K.S.; Wee, M.; Haron, F.F.; Patra, A.; Nayan, N.; Soon, C.F.J.P.C.; Processing, P. Effects of Oxygen (O₂) Plasma Treatment in Promoting the Germination and Growth of Chili. *Plasma Chem. Plasma Process.* **2022**, *42*, 91–108. [[CrossRef](#)]
20. Siow, K.S.; Britcher, L.; Kumar, S.; Griesser, H.J. QCM-D and XPS study of protein adsorption on plasma polymers with sulfonate and phosphonate surface groups. *Colloids Surf. B Biointerfaces* **2019**, *173*, 447–453. [[CrossRef](#)]
21. Ahmed, N.; Masood, A.; Siow, K.S.; Wee, M.; Auliya, R.Z.; Ho, W.K.J.A. Effect of H₂O-based low-pressure plasma (LPP) treatment on the germination of bambara groundnut seeds. *Agronomy* **2021**, *11*, 338. [[CrossRef](#)]
22. Madkour, A.E.; Tew, G.N. Towards self-sterilizing medical devices: Controlling infection. *Polym. Int.* **2008**, *57*, 6–10. [[CrossRef](#)]
23. Moyes, R.B.; Reynolds, J.; Breakwell, D.P. Differential staining of bacteria: Gram stain. *Curr. Protoc. Microbiol.* **2009**, *15*, A.3C.1–A.3C.8. [[CrossRef](#)]
24. Wang, Y.; Xiao, J.; Suzek, T.O.; Zhang, J.; Wang, J.; Bryant, S.H. PubChem: A public information system for analyzing bioactivities of small molecules. *Nucleic Acids Res.* **2009**, *37*, W623–W633. [[CrossRef](#)] [[PubMed](#)]
25. Bode, J.W. Reactor ChemAxon Ltd.: Maramaros koz 2/a, Budapest, 1037 Hungary. Contact ChemAxon for Pricing Information. ACS Publications. 2004. Available online: www.chemaxon.com (accessed on 10 January 2023).
26. Wang, X.; Guan, Q.; Wang, X.; Teng, D.; Mao, R.; Yao, J.; Wang, J. Paving the way to construct a new vaccine against *Escherichia coli* from its recombinant outer membrane protein C via a murine model. *Process Biochem.* **2015**, *50*, 1194–1201. [[CrossRef](#)]

27. Confer, A.W.; Ayalew, S. The OmpA family of proteins: Roles in bacterial pathogenesis and immunity. *Vet. Microbiol.* **2013**, *163*, 207–222. [[CrossRef](#)] [[PubMed](#)]
28. Burley, S.K.; Berman, H.M.; Kleywegt, G.J.; Markley, J.L.; Nakamura, H.; Velankar, S. Protein Data Bank (PDB): The single global macromolecular structure archive. In *Protein Crystallography: Methods and Protocols*; Humana Press: New York, NY, USA, 2017; pp. 627–641.
29. Liu, Y.; Grimm, M.; Dai, W.-t.; Hou, M.-c.; Xiao, Z.-X.; Cao, Y. CB-Dock: A web server for cavity detection-guided protein–ligand blind docking. *Acta Pharmacol. Sin.* **2020**, *41*, 138–144. [[CrossRef](#)]
30. Starič, P.; Grobelnik Mlakar, S.; Junkar, I. Response of Two Different Wheat Varieties to Glow and Afterglow Oxygen Plasma. *Plants* **2021**, *10*, 1728. [[CrossRef](#)]
31. Kolská, Z.; Makajová, Z.; Kolářová, K.; Slepícková, N.K.; Trostová, S.; Řezníčková, A.; Siegel, J.; Švorčík, V. Electrokinetic potential and other surface properties of polymer foils and their modifications. *Polym. Sci.* **2013**, *4*, 203–228.
32. Ajdnik, U.; Zemljič, L.F.; Plohl, O.; Pérez, L.; Trček, J.; Bračič, M.; Mohan, T. Bioactive Functional Nanolayers of Chitosan–Lysine Surfactant with Single- and Mixed-Protein-Repellent and Antibiofilm Properties for Medical Implants. *ACS Appl. Mater. Interfaces* **2021**, *13*, 23352–23368. [[CrossRef](#)]
33. Rzhepishevskaya, O.; Hakobyan, S.; Ruhel, R.; Gautrot, J.; Barbero, D.; Ramstedt, M. The surface charge of anti-bacterial coatings alters motility and biofilm architecture. *Biomater. Sci.* **2013**, *1*, 589–602. [[CrossRef](#)]
34. Srinivasan, S.; McKinley, G.H.; Cohen, R.E. Assessing the accuracy of contact angle measurements for sessile drops on liquid-repellent surfaces. *Langmuir* **2011**, *27*, 13582–13589. [[CrossRef](#)]
35. Wang, Y.; Sang, D.K.; Du, Z.; Zhang, C.; Tian, M.; Mi, J. Interfacial structures, surface tensions, and contact angles of diiodomethane on fluorinated polymers. *J. Phys. Chem. C* **2014**, *118*, 10143–10152. [[CrossRef](#)]
36. Belibel, R.; Avramoglou, T.; Garcia, A.; Barbaud, C.; Mora, L. Effect of chemical heterogeneity of biodegradable polymers on surface energy: A static contact angle analysis of polyester model films. *Mater. Sci. Eng. C* **2016**, *59*, 998–1006. [[CrossRef](#)]
37. Fahmy, A.; Mix, R.; Schönhals, A.; Friedrich, J. Surface and bulk structure of thin spin coated and plasma-polymerized polystyrene films. *Plasma Chem. Plasma Process.* **2012**, *32*, 767–780. [[CrossRef](#)]
38. Kuchakova, I.; Ionita, M.D.; Ionita, E.-R.; Lazea-Stoyanova, A.; Brajnicov, S.; Mitu, B.; Dinescu, G.; De Vrieze, M.; Cvelbar, U.; Zille, A.; et al. Atmospheric Pressure Plasma Deposition of Organosilicon Thin Films by Direct Current and Radio-frequency Plasma Jets. *Materials* **2020**, *13*, 1296. [[CrossRef](#)] [[PubMed](#)]
39. Shenton, M.J.; Lovell-Hoare, M.C.; Stevens, G.C. Adhesion enhancement of polymer surfaces by atmospheric plasma treatment. *J. Phys. D Appl. Phys.* **2001**, *34*, 2754. [[CrossRef](#)]
40. Baer, D.R.; Gaspar, D.J.; Nachimuthu, P.; Techane, S.D.; Castner, D.G. Application of surface chemical analysis tools for characterization of nanoparticles. *Anal. Bioanal. Chem.* **2010**, *396*, 983–1002. [[CrossRef](#)]
41. Dardar, H.; Belbachir, M.; Harrane, A. A green synthesis of polylimonene using Maghnite-H⁺, an exchanged montmorillonite clay, as eco-catalyst. *Bull. Chem. React. Eng. Catal.* **2019**, *14*, 69–78. [[CrossRef](#)]
42. Gerchman, D.; Bones, B.; Pereira, M.; Takimi, A. Thin film deposition by plasma polymerization using d-limonene as a renewable precursor. *Prog. Org. Coat.* **2019**, *129*, 133–139. [[CrossRef](#)]
43. Lin-Vien, D.; Colthup, N.B.; Fateley, W.G.; Grasselli, J.G. *The Handbook of Infrared and Raman Characteristic Frequencies of Organic Molecules*; Elsevier: Amsterdam, The Netherlands, 1991.
44. Clouet, F.; Shi, M. Interactions of polymer model surfaces with cold plasmas: Hexatriacontane as a model molecule of high-density polyethylene and octadecyl octadecanoate as a model of polyester. I. Degradation rate versus time and power. *J. Appl. Polym. Sci.* **1992**, *46*, 1955–1966. [[CrossRef](#)]
45. Bazaka, K.; Jacob, M.V. Post-deposition ageing reactions of plasma derived polyterpenol thin films. *Polym. Degrad. Stab.* **2010**, *95*, 1123–1128. [[CrossRef](#)]
46. Siow, K.S.; Britcher, L.; Kumar, S.; Griesser, H.J. Plasma Polymers Containing Sulfur and Their Co-Polymers With 1, 7-Octadiene: Chemical and Structural Analysis. *Plasma Process. Polym.* **2017**, *14*, 1600044. [[CrossRef](#)]
47. Alancherry, S.; Bazaka, K.; Jacob, M.V. RF plasma polymerization of orange oil and characterization of the polymer thin films. *J. Polym. Environ.* **2018**, *26*, 2925–2933. [[CrossRef](#)]
48. Ahmad, J.; Bazaka, K.; Whittle, J.D.; Michelmor, A.; Jacob, M.V. Structural Characterization of γ -Terpinene Thin Films Using Mass Spectroscopy and X-ray Photoelectron Spectroscopy. *Plasma Process. Polym.* **2015**, *12*, 1085–1094. [[CrossRef](#)]
49. Park, C.-S.; Jung, E.Y.; Kim, D.H.; Kim, D.Y.; Lee, H.-K.; Shin, B.J.; Lee, D.H.; Tae, H.-S. Atmospheric pressure plasma polymerization synthesis and characterization of polyaniline films doped with and without iodine. *Materials* **2017**, *10*, 1272. [[CrossRef](#)]
50. Diu, T.; Faruqui, N.; Sjöström, T.; Lamarre, B.; Jenkinson, H.F.; Su, B.; Ryadnov, M.G. Cicada-inspired cell-instructive nanopatterned arrays. *Sci. Rep.* **2014**, *4*, 7122. [[CrossRef](#)]
51. Schiffman, J.D.; Elimelech, M. Antibacterial activity of electrospun polymer mats with incorporated narrow diameter single-walled carbon nanotubes. *ACS Appl. Mater. Interfaces* **2011**, *3*, 462–468. [[CrossRef](#)] [[PubMed](#)]
52. Lee, S.B.; Koepsel, R.R.; Morley, S.W.; Matyjaszewski, K.; Sun, Y.; Russell, A.J. Permanent, nonleaching antibacterial surfaces. 1. Synthesis by atom transfer radical polymerization. *Biomacromolecules* **2004**, *5*, 877–882. [[CrossRef](#)]
53. Robertson, J.; McGoverin, C.; White, J.R.; Vanholsbeeck, F.; Swift, S. Rapid detection of *Escherichia coli* antibiotic susceptibility using live/dead spectrometry for lytic agents. *Microorganisms* **2021**, *9*, 924. [[CrossRef](#)] [[PubMed](#)]

54. Kumar, V.; Pulpytel, J.; Giudetti, G.; Rauscher, H.; Rossi, F.; Arefi-Khonsari, F. Amphiphilic Copolymer Coatings via Plasma Polymerisation Process: Switching and Anti-Biofouling Characteristics. *Plasma Process. Polym.* **2011**, *8*, 373–385. [[CrossRef](#)]
55. Vijesh, A.; Isloor, A.M.; Telkar, S.; Arulmoli, T.; Fun, H.-K. Molecular docking studies of some new imidazole derivatives for antimicrobial properties. *Arab. J. Chem.* **2013**, *6*, 197–204. [[CrossRef](#)]
56. Liu, Y.-F.; Yan, J.-J.; Lei, H.-Y.; Teng, C.-H.; Wang, M.-C.; Tseng, C.-C.; Wu, J.-J. Loss of outer membrane protein C in *Escherichia coli* contributes to both antibiotic resistance and escaping antibody-dependent bactericidal activity. *Infect. Immun.* **2012**, *80*, 1815–1822. [[CrossRef](#)] [[PubMed](#)]
57. Kouranov, A.; Xie, L.; de la Cruz, J.; Chen, L.; Westbrook, J.; Bourne, P.E.; Berman, H.M. The RCSB PDB information portal for structural genomics. *Nucleic Acids Res.* **2006**, *34*, D302–D305. [[CrossRef](#)] [[PubMed](#)]
58. Kim, S.; Thiessen, P.A.; Bolton, E.E.; Chen, J.; Fu, G.; Gindulyte, A.; Han, L.; He, J.; He, S.; Shoemaker, B.A. PubChem substance and compound databases. *Nucleic Acids Res.* **2016**, *44*, D1202–D1213. [[CrossRef](#)]
59. Eberhardt, J.; Santos-Martins, D.; Tillack, A.F.; Forli, S. AutoDock Vina 1.2. 0: New docking methods, expanded force field, and python bindings. *J. Chem. Inf. Model.* **2021**, *61*, 3891–3898. [[CrossRef](#)] [[PubMed](#)]

Disclaimer/Publisher’s Note: The statements, opinions and data contained in all publications are solely those of the individual author(s) and contributor(s) and not of MDPI and/or the editor(s). MDPI and/or the editor(s) disclaim responsibility for any injury to people or property resulting from any ideas, methods, instructions or products referred to in the content.